



Friction properties and deformation mechanisms of halite(-mica) gouges from low to high sliding velocities



Loes Buijze^{a,b,c,*}, André R. Niemeijer^a, Raehee Han^{c,2}, Toshihiko Shimamoto^{c,3}, Christopher J. Spiers^a

^a HPT Laboratory, Faculty of Geoscience, Utrecht University, Budapestlaan 4, 3584 CD, Utrecht, The Netherlands

^b Netherlands Organisation for Applied Scientific Research – TNO, Princetonlaan 6, 3584 CB, Utrecht, The Netherlands

^c Department of Earth and Planetary Systems Science, Graduate School of Science, Hiroshima University, 1-3-1 Kagami-yama, Higashi Hiroshima 739-8526, Japan

ARTICLE INFO

Article history:

Received 8 March 2016

Received in revised form 12 September 2016

Accepted 15 September 2016

Available online 9 November 2016

Editor: P. Shearer

Keywords:

halite

low to high velocity friction

rotary shear apparatus

ABSTRACT

The evolution of friction as a function of slip rate is important in understanding earthquake nucleation and propagation. Many laboratory experiments investigating friction of fault rocks are either conducted in the low velocity regime (10^{-8} – 10^{-4} m s^{-1}) or in the high velocity regime (0.01 – 1 m s^{-1}). Here, we report on the evolution of friction and corresponding operating deformation mechanisms in analog gouges deformed from low to high slip rates, bridging the gap between these low and high velocity regimes. We used halite and halite-muscovite gouges to simulate processes, governing friction, active in upper crustal quartzitic fault rocks, at conditions accessible in the laboratory. The gouges were deformed over a 7 orders of magnitude range of slip rate (10^{-7} – 1 m s^{-1}) using a low-to-high velocity rotary shear apparatus, using a normal stress of 5 MPa and room-dry humidity. Microstructural analysis was conducted to study the deformation mechanisms. Four frictional regimes as a function of slip rate could be recognized from the mechanical data, showing a transitional regime and stable sliding (10^{-7} – 10^{-6} m s^{-1}), unstable sliding and weakening (10^{-6} – 10^{-3} m s^{-1}), hardening (10^{-2} – 10^{-1} m s^{-1}) and strong weakening (10^{-1} – 1 m s^{-1}). Each of the four regimes can be associated with a distinct microstructure, reflecting a transition from mainly brittle deformation accompanied by pressure solution healing to temperature activated deformation mechanisms. Additionally, the frictional response of a sliding gouge to a sudden acceleration of slip rate to seismic velocities was investigated. These showed an initial strengthening, the amount of which depended on the friction level at which the step was made, followed by strong slip weakening.

© 2016 Elsevier B.V. All rights reserved.

1. Introduction

Variations in fault friction are key in understanding and modeling of the seismic cycle. Friction on a sliding surface or within a gouge can be described by the empirical laboratory-derived rate-and-state friction laws (Dieterich, 1979; Ruina, 1983). Frictional strength may increase with increasing velocity ($a - b > 0$, stable

sliding), or decrease with increasing velocity ($a - b < 0$), which is a requirement for an earthquake instability to develop (Ruina, 1983). Implementation of these rate-and-state friction models in (quasi-) dynamic fault modeling of crustal-scale faults has reproduced many phenomena observed in the seismic cycle, such as preseismic slip, the nucleation and propagation of instabilities, coseismic, interseismic fault healing and seismic transients (e.g. Lapusta et al., 2000; Ben-Zion and Rice, 1997). Including an ($a - b$) value which varies with velocity in sign (e.g. Shibasaki and Shimamoto, 2007; Hawthorne and Rubin, 2013) can have large effects on the rupture characteristics. For our understanding of the mechanisms of seismicity, it is thus important to investigate how friction and its velocity dependence, ($a - b$), evolve over the entire range of slip rates relevant to the seismic cycle, and to understand the controlling processes to allow for more reliable extrapolation of laboratory data to nature.

Laboratory experiments at slow slip velocities (< 100 $\mu\text{m s}^{-1}$) and mostly small displacements (10^{-3} – 10^{-2} m s^{-1}) formed the

* Corresponding author.

E-mail addresses: loes.buijze@tno.nl (L. Buijze), a.r.niemeijer@uu.nl (A.R. Niemeijer), raeheehan@gnu.ac.kr (R. Han), shima_kyoto@yahoo.co.jp (T. Shimamoto), c.j.spiers@uu.nl (C.J. Spiers).

¹ Present address: HPT Laboratory, Faculty of Geoscience, Utrecht University, Budapestlaan 4, 3584 CD, Utrecht, The Netherlands.

² Now at: Department of Geology and Research Institute of Natural Science, Gyeongsang National University, Jinju 52828, Republic of Korea.

³ Now at: State Key Laboratory of Earthquake Dynamics, Institute of Geology, China Earthquake Administration, Beijing 100-029, China.

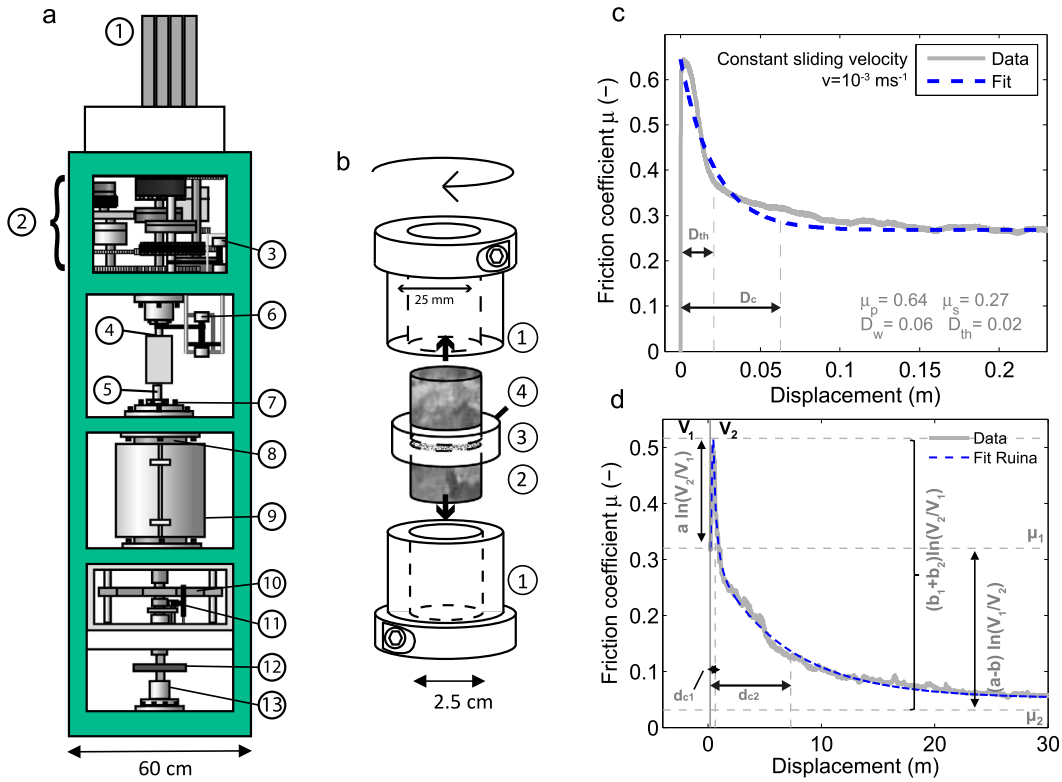


Fig. 1. Deformation apparatus, sample assembly and data fits used in this study. a) Schematic drawing of the low-to-high velocity rotary shear apparatus. 1) servo-motor, 2) gear and belt systems that drives the rotary column, 3) rotary encoder, 4) rotary shaft, 5) stationary column, 6) rotary potentiometer, 7) spherical plate for alignment of stationary column, 8) pressure vessel, 9) external furnace, 10) torque gauge, 11) LVDT, 12) axial force gauge and 13) hydraulic jack (buffered by gas pressure) for applying the normal load via the stationary shaft. The place where the sample assembly (b) is located in the machine is indicated by the rectangular area between 4 and 5. b) Sample assembly with 1) shaft lock system to grip the gabbro pistons and connect to the stationary and rotary shaft, 2) gabbro piston, 3) Teflon sleeve, 4) gouge layer. c) Exponential fit of representative experimental data using Equation (1), with μ_p : peak friction coefficient, μ_s : steady state friction coefficient, D_w : slip weakening distance, D_{th} : thermal weakening distance. d) Fit of a representative velocity stepping experiment with a two-state-variable rate-and-state friction law (Equations (2) and (4)), with V_1 : initial sliding velocity (here 10^{-3} ms^{-1}), V_2 : sliding velocity after the step change (here 1 ms^{-1}), a, b ($= b_1 + b_2$): rate-and-state parameters, d_{c1}, d_{c2} : critical slip distances, μ_1 : steady state friction coefficient at V_1 , μ_2 : steady state friction coefficient at V_2 .

basis of the rate-and-state friction model mentioned above. Fault rocks have been deformed under a wide range of conditions (e.g. varying normal stress, temperature, fluid content, grain size, wall-rock roughness) at these velocities (e.g. Marone, 1998). The frictional changes observed in these experiments due to imposed slip or velocity changes are mostly small. On the other hand, high-velocity ($0.1\text{--}1 \text{ ms}^{-1}$) rotary shear experiments with up to 10's of meters of displacement revealed extreme weakening of more than 90% of the friction for various rock types (Tsutsumi and Shimamoto, 1997; Di Toro et al., 2011). Data on friction at intermediate velocities are scarce, although recently a number of studies collected frictional data covering velocities from $100 \mu\text{s}^{-1}$ to 0.1 ms^{-1} (Ferri et al., 2011; Reches and Lockner, 2010; Di Toro et al., 2011; Liao et al., 2014). Here we deformed fault gouges in a rotary shear apparatus at constant velocities ranging from 10^{-7} ms^{-1} to 1 ms^{-1} . Also, we investigate the frictional response to a sudden acceleration (e.g. simulating an advancing rupture front with a short rise time on a fault sliding at slower slip rates) by stepping up the velocity two to three orders of magnitude to velocities of 0.1 to 1 ms^{-1} . We checked whether the frictional response could be modeled with rate-and-state friction theory, as is conventional for slower slip rate stepping experiments.

In the high-velocity apparatus, a (gouge) material cannot be deformed at the in-situ P–T conditions acting on upper crustal faults, due to limitations in normal stress and temperature that can be applied. Hence, the appropriate deformation processes controlling deformation at the in-situ conditions may not be activated. To study a material deforming via processes active in the upper crust, but at conditions accessible in the apparatus, we used halite and

halite–muscovite gouges as a material analog to (phyllosilicate-containing) quartzitic fault rock, following Niemeijer and Spiers (2006). Earlier experiments have shown that these gouges produce microstructures which resemble those found in nature, both at low (Bos et al., 2000a; Niemeijer and Spiers, 2005; Niemeijer et al., 2010; Shimamoto, 1985; Hiraga and Shimamoto, 1987; Chester and Logan, 1990) and high velocities (Kim et al., 2010). Here, we deformed both halite and halite–muscovite gouge at velocities from 10^{-7} ms^{-1} to 1 ms^{-1} , at a normal stress of 5 MPa, and study both the mechanical data and the resulting microstructures to identify the processes controlling the deformation.

2. Experimental procedure methods

2.1. Sample material

In each experiment 1 g of analytical grade halite or mixed halite–muscovite (80:20) was used. The halite was sieved to achieve a halite grain size of $<106 \mu\text{m}$, and the muscovite (mined in Aspang, Austria, Internatio B. V.) had a median grain size of $13 \mu\text{m}$.

2.2. Deformation apparatus, sample assembly and experimental procedure

We performed friction experiments in the low-to-high velocity rotary shear apparatus at Hiroshima University (Togo and Shimamoto, 2012 for detailed machine specifications) (Fig. 1a). The gouge was sandwiched between two solid gabbro cylinders

(Fig. 1b) with a diameter of 25 mm whose surfaces were roughened with #120 SiC powder. A Teflon ring on the outside of the gabbro pistons prevented lateral extrusion of the gouge. The gabbro pistons were connected to the vertical drive shafts by a shaft lock system. Torque was applied to the sample via the top rotary shaft (#4 in Fig. 1a), which is connected to a gear-and-belt motor system. Before each experimental run, the top piston was centered to within 5 μm to ensure good alignment. Normal load was applied via the bottom shaft by means of a gas pressure system; due to this loading technique it could however vary by up to 10% during the longer (lasting for hours) experiments. Torque was measured using two beam-type torque gauges connected to the stationary shaft at the bottom (#10 in Fig. 1a) to within 0.001 N m, and axial force (kN) was measured by an axial force gauge to within 0.003 kN (#12 in Fig. 1a). Vertical displacement due to sample shortening or dilatation was measured with an accuracy of 3 nm by an LVDT which was attached to the stationary shaft (#11 in Fig. 1a). Logging rates ranged up to 200 Hz depending on the driving velocity.

Constant velocity tests were performed in the range 10^{-7} to 1 ms^{-1} on both halite and halite–muscovite gouges, at a normal stress of 5 MPa and room temperature. The gouges were room-dry (humidity $\sim 70\%$), but moisture may be present in the sample. To investigate the transient frictional properties of the halite–muscovite mixture, the velocity was changed in six experiments, which were performed in the high velocity regime (10^{-3} – 1 ms^{-1}). The velocity changes were applied when steady state was reached at the initial velocity, and the velocity change was up to three orders of magnitude.

2.3. Data processing

The measured torque and axial load were converted to shear τ and normal stresses σ_n using the sample area, with friction coefficient $\mu = \tau/\sigma$, ignoring cohesion. Assuming constant shear stress across the sample, an equivalent velocity v_{eq} was defined following (Tsutsumi and Shimamoto, 1997), hereafter termed velocity v , the integration of which gives the displacement d .

For constant velocity experiments we fitted the evolution of friction after reaching its peak value with an exponential function of the form

$$\mu = \mu_s + (\mu_p - \mu_s) \exp(Cd) \quad (1)$$

Here μ_s is the steady state coefficient of friction, μ_p the peak coefficient of friction, and d the displacement. C is a factor that gives the slip weakening distance D_w as $C = \ln(0.05)/D_w$ (Mizoguchi et al., 2007), which is the distance over which friction falls 95% of the total friction drop, and the thermal weakening distance D_{th} as $C = -1/D_{th}$ (Di Toro et al., 2011), which is the distance over which friction falls to $1/e$ of the total friction drop. In some cases, the data could not adequately be described by (1) so we manually determined D_w (95% friction drop) and D_{th} ($1/e$ friction decrease) from the smoothed friction-displacement curve.

The rate-and-state behavior of the velocity stepping experiments was examined using, in a generalized form (Dieterich, 1979; Ruina, 1983)

$$\mu = \mu_1 + a \ln\left(\frac{V_2}{V_1}\right) + b_i \left(\frac{V_1 \theta_i}{d_{ci}}\right) \quad (2)$$

where V_1 and μ_1 are the reference velocity and reference coefficient of friction, V_2 is the velocity after the step change, θ_i is one or more state variables related to the history and evolution of the slip surface, d_{ci} is the characteristic slip distance describing the length over which the state variable(s) acts and a and b_i are scaling parameters of, respectively the direct and evolution effect,

which together describe the magnitude of the friction change at steady state due to a step change in velocity

$$(a - b) = \frac{\Delta \mu_s}{\Delta \ln V} \quad (3)$$

The value of $(a - b)$ indicates if a material is velocity weakening ($a - b < 0$, potentially unstable) or velocity strengthening ($a - b > 0$, stable). The state variable can be described by either the slip law (Ruina, 1983)

$$\frac{\delta \theta_i}{\delta t} = - \left(\frac{V \theta_i}{d_{ci}} \right) \ln \left(\frac{V \theta_i}{d_{ci}} \right) \quad (4)$$

or the aging law (Dieterich, 1979)

$$\frac{\delta \theta_i}{\delta t} = 1 - \left(\frac{V \theta_i}{d_{ci}} \right) \quad (5)$$

Modeling of the velocity steps performed in this study required the use of a two state-variable friction law ($i = 2$) (e.g. Blanpied et al., 1998). For a two state variable friction law there are 5 constitutive parameters in total: a , b_1 , b_2 , d_{c1} and d_{c2} . Interactions between the velocity dependence of the sample and the stiffness of the machine have to be taken into account and it is approximated by $d\mu/dt = k(V_1 - V_2)$ (Reinen and Weeks, 1993) where k is the stiffness of the machine. To solve the rate-and-state friction laws in combination with this equation relating the stiffness and velocity dependence, a fifth-order Runge–Kutta scheme with adaptive time stepping was used. The constitutive parameters are obtained by using an iterative least squares method described in (Reinen and Weeks, 1993). An example of a velocity stepping experiment and the resulting rate-and-state fit using the slip law is shown in Fig. 1d.

2.4. Microstructural analysis

After an experiment, the sample assembly was removed from the machine and the Teflon ring was slid down, exposing the gouge layer and allowing it to be impregnated with epoxy, and the sample was left to dry in a vacuum container. To produce thin sections, samples were cut perpendicular to the gouge layer at $\sim 3 \text{ mm}$ from the circumferential surface of the gabbro cores, using oil as lubricant. Thin sections were studied in an XL30S Scanning Electron Microscope. Some sections were etched and investigated under the optical microscope using reflected light.

3. Results

3.1. Mechanical behavior at constant slip rate

The evolution of the coefficient of friction and compaction with shear displacement is shown for a representative selection of the constant velocity experiments on both pure and mixed gouge (Fig. 2). All results (except slip-hardening ones) were fit with Equation (1) to obtain μ_s , the thermal slip distance D_{th} , the slip weakening distance D_w (see Table 1a for summary, experimental conditions and fitted parameters).

All samples showed an initial quasi-elastic loading stage up to the peak friction coefficient (μ_p), accompanied by rapid compaction (axial shortening). For the lowest velocity runs hdr622 (10^{-7} ms^{-1}), hdr616 (10^{-6} ms^{-1}), and hdr608 (10^{-6} ms^{-1}), compaction switched to dilatation before μ_p was reached, but started compacting again at 1.5–2 mm of slip when μ_p was attained and weakening initiated (Fig. 2a). Pure halite samples hdr622 and hdr616 weakened with slip immediately after overcoming a μ_p (0.9) but after $\sim 5 \text{ mm}$ started to harden again to a μ of ~ 0.8 . The mixed sample hdr608 on the other hand had a lower

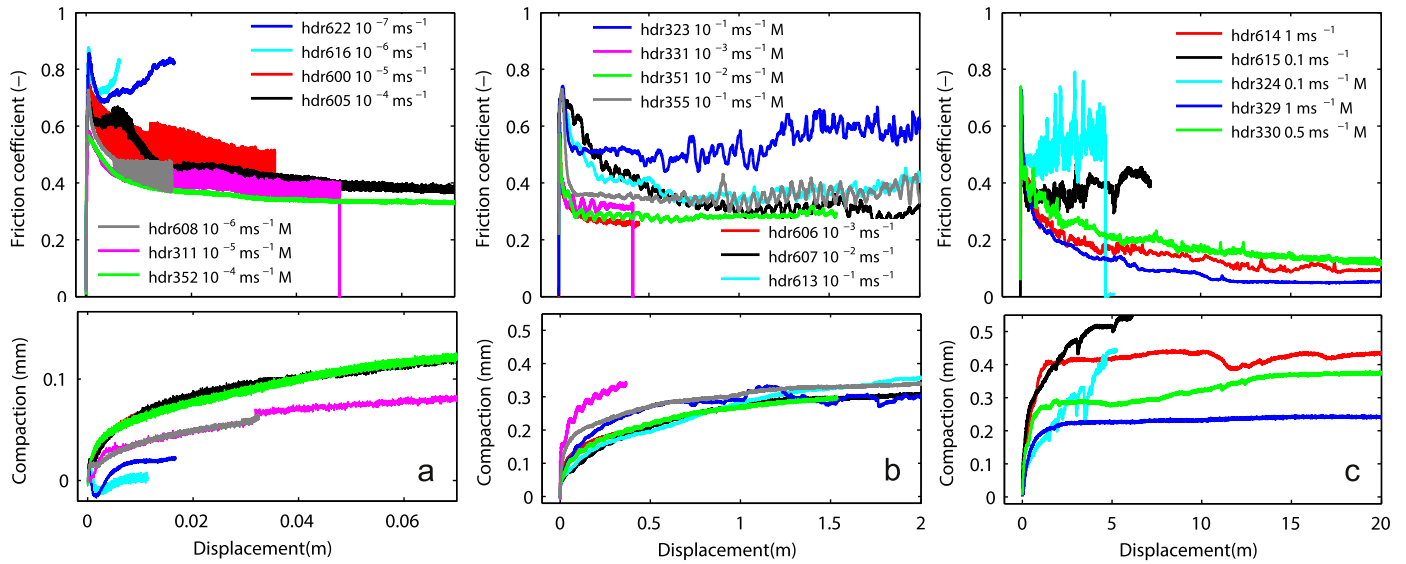


Fig. 2. Evolution of friction and compaction behavior of a representative set of experiments on both halite and halite-muscovite gouges. Gouges were deformed at a) slow slip rates from $0.1 \mu\text{m s}^{-1}$ to $100 \mu\text{m s}^{-1}$, b) intermediate slip rates from 1 mm s^{-1} to 0.01 mm s^{-1} and c) fast slip rates from 0.01 mm s^{-1} to 1 mm s^{-1} . The applied normal stress in all experiments is 5 MPa and experiments were conducted at room temperature and room-humidity. The starting thickness of the gouge is $\sim 1 \text{ mm}$. The M in the legend denotes the gouges which contain 20% muscovite.

Table 1

Summary of constant velocity experiments and fitted parameters. With gouge compositions ha: halite, ha-mu: 80% halite, 20% muscovite, V_1 : the shear velocity, total d : total displacement, μ_p : peak friction, μ_s : steady-state friction coefficient, D_w : slip weakening distance (95% of friction drop), and D_{th} : thermal slip weakening distance ($1 - 1/e$ friction drop). The μ_s , D_w , and D_{th} were determined from fits with Equation (1). S-s (y) indicates whether stick-slip was observed during the experiment. All experiments were conducted at 5 MPa normal stress, room-humidity and room temperature.

Run #	Gouge	V_1 (m s^{-1})	Total d (m)	μ_p (–)	μ_s (–)	D_w (m)	D_{th} (m)	s-s?
hdr622	ha	$1.00\text{E}-07$	0.017	0.86	0.68 ^a	–	–	–
hdr616	ha	$6.10\text{E}-07$	0.006	0.88	0.71 ^a	–	–	–
hdr600	ha	$9.96\text{E}-06$	0.036	0.77	0.50	0.009	0.003	y
hdr605	ha	$9.99\text{E}-05$	0.123	0.70	0.36	0.047	0.016	y
hdr606	ha	$1.00\text{E}-03$	0.445	0.64	0.27	0.063	0.021	y
hdr607	ha	$1.01\text{E}-02$	3.391	0.70	0.33	0.743	0.248	–
hdr613	ha	$1.00\text{E}-01$	7.778	0.68	0.39	0.324	0.108	–
hdr615	ha	$1.00\text{E}-01$	7.229	0.65	0.38	0.233	0.078	–
hdr614	ha	$1.00\text{E}+00$	43.798	0.64	0.07 ^b	14.072 ^b	1.451 ^b	–
hdr608	ha-mu	$6.10\text{E}-07$	0.016	0.73	0.44	0.006	0.002	y
hdr316	ha-mu	$1.09\text{E}-06$	0.039	0.66	0.46	0.035	0.012	y
hdr311	ha-mu	$9.59\text{E}-06$	0.048	0.58	0.39	0.012	0.004	y
hdr312	ha-mu	$9.59\text{E}-05$	0.086	0.62	0.34	0.013	0.004	y
hdr352	ha-mu	$9.59\text{E}-05$	0.087	0.57	0.33	0.023	0.008	y
hdr601	ha-mu	$1.00\text{E}-04$	0.092	0.64	0.46	0.036	0.012	y
hdr331	ha-mu	$1.00\text{E}-03$	0.417	0.57	0.31	0.052	0.018	–
hdr334	ha-mu	$1.00\text{E}-03$	0.989	0.60	0.30	0.052	0.017	–
hdr351	ha-mu	$1.00\text{E}-02$	1.539	0.57	0.28	0.076	0.025	–
hdr353	ha-mu	$1.00\text{E}-02$	1.204	0.54	0.28	0.099	0.033	–
hdr354	ha-mu	$5.00\text{E}-02$	2.068	0.71	0.36	0.071	0.024	–
hdr355	ha-mu	$5.01\text{E}-02$	4.498	0.73	0.40	0.045	0.015	–
hdr324	ha-mu	$1.00\text{E}-01$	5.242	0.72	0.47	0.088	0.030	–
hdr323	ha-mu	$1.00\text{E}-01$	5.019	0.74	0.50	0.064	0.025	–
hdr330	ha-mu	$5.00\text{E}-01$	22.967	0.74	0.12 ^b	12.333 ^b	1.060 ^b	–
hdr329	ha-mu	$1.00\text{E}+00$	20.559	0.73	0.06 ^b	8.103 ^b	0.885 ^b	–

^a Experiments show hardening, the μ_s shown here is the lowest value measured after peak friction.

^b Experiments could not be fit properly with Equation (1), and parameters were picked manually from smoothed data.

μ_p of 0.72 and showed continuous weakening after overcoming μ_p until after 12 mm of displacement stick-slips started to occur, evolving to a significantly lower steady state friction coefficient (μ_s) of 0.45. At velocities of 10^{-5} – 10^{-4} m s^{-1} both the pure halite (hdr600) and mixed gouge samples (hdr311 and hdr352) weakened rapidly beyond μ_p and exhibited stick-slip behavior, with the largest amplitudes at the smallest velocities. No net dilatation occurred in these samples, but a stage of reduced compaction occurred around the peak friction, then increasing again with displacement.

The μ_s ranged from 0.35–0.5 and decreased with increasing velocity, and was lower for mixed gouges than the pure halite at the same velocity. Typical μ_p of pure halite was 0.75–0.88 and for mixed gouge 0.55–0.72, also decreasing with velocity.

The μ_s increased for samples deformed at constant velocities in the range 10^{-3} m s^{-1} – 10^{-1} m s^{-1} (Fig. 2b). For pure halite samples, μ_s increased with increasing velocity from 0.27 at 10^{-3} m s^{-1} to 0.38 at 0.1 m s^{-1} (hdr613, Fig. 2b and hdr615, Fig. 2c). For mixed samples μ_s first decreased from 10^{-3} m s^{-1}

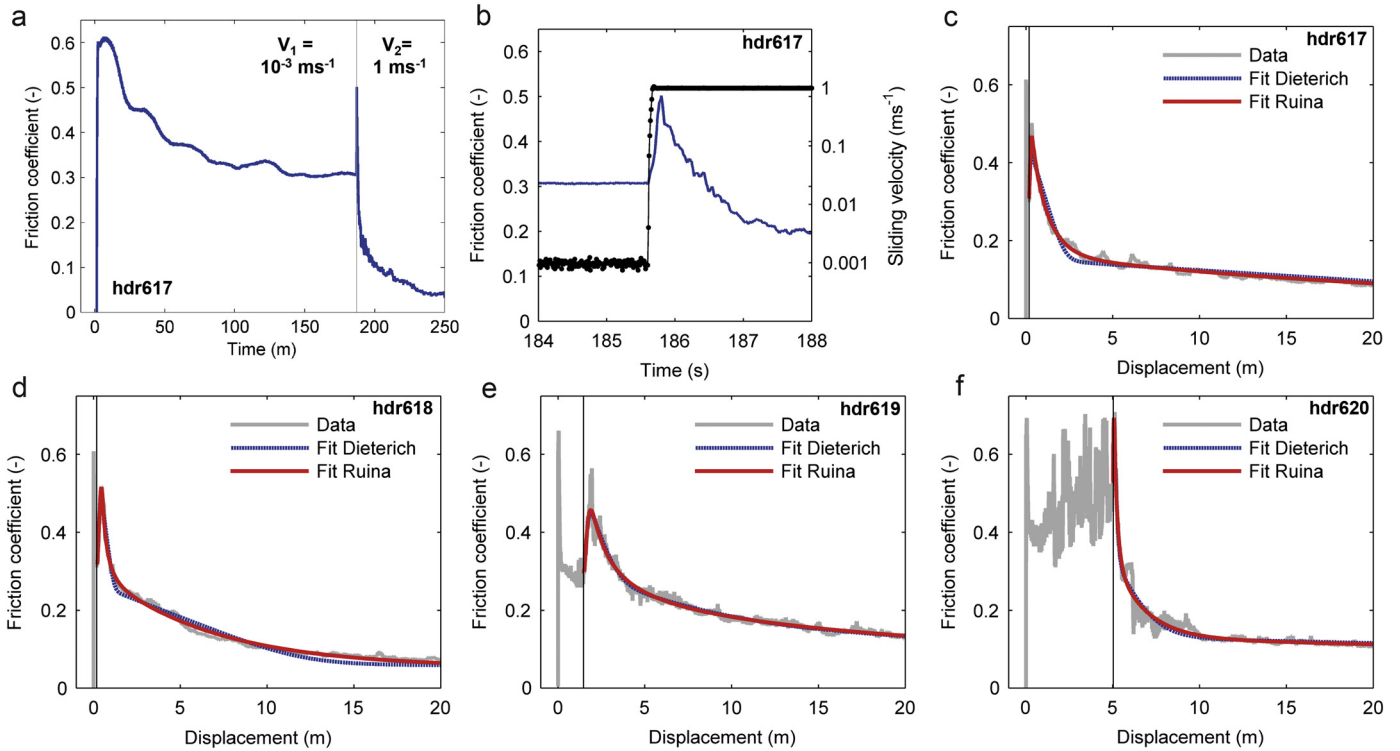


Fig. 3. Velocity stepping experiments and fits with a two-state-variable rate-and-state friction model. a) Overview of whole experiment hdr617 as a function of time, with a velocity step from 10^{-3} to 0.98 ms^{-1} , b) zoom of the velocity jump with the friction coefficient (blue) and the slip rate (black), c) hdr617 (1×10^{-3} to $8.7 \times 10^{-1} \text{ ms}^{-1}$) data (grey) and RSF fits, d) hdr617 (1×10^{-3} to $9.8 \times 10^{-1} \text{ ms}^{-1}$) data and fits, e) hdr619 (3×10^{-2} to $4.7 \times 10^{-1} \text{ ms}^{-1}$), and f) hdr620 (7×10^{-2} to $5.1 \times 10^{-1} \text{ ms}^{-1}$). The fits with the slip law (Ruina) is indicated in red, the aging law (Dieterich) by the blue dashed line. Fitted parameters can be found in Table 2. (For interpretation of the references to color in this figure legend, the reader is referred to the web version of this article.)

to 10^{-2} ms^{-1} , but increased then increased to 0.5 at 10^{-1} ms^{-1} (hdr323) (Fig. 2c). Weakening to μ_s occurred over a larger displacement for pure halite samples hdr607 (10^{-2} ms^{-1}) and hdr613 (10^{-2} ms^{-1}) than for their mixed gouge equivalent.

At slip rates around 0.1 ms^{-1} , oscillations related to (small) misalignment of the sample assembly became more prominent in the data. Also the data became more irregular, showing periods of weakening and restrengthening, unrelated to the period of one rotation. Compaction was larger than in the slower experiments ($0.3\text{--}0.4 \text{ mm}$) and no dilatation or reduced compaction rate was observed in the early stages of any of the samples. The larger compaction may in part reflect the gouge extrusion which occurred in particular in the 10^{-1} ms^{-1} samples.

At the largest slip rates investigated ($0.5\text{--}1 \text{ ms}^{-1}$) frictional strength showed an extreme reduction in all samples, reaching steady state values as low as 0.05 in case of the halite-muscovite sample deformed at 1 ms^{-1} (hdr329). Sample hdr330 (0.5 ms^{-1}) displayed some brief periods of re-strengthening in the first few m displacement. Pure halite (hdr614) showed more compaction than mixed gouge samples hdr330 and hdr329 and was slightly stronger with a μ_s of 0.08. In the 1 ms^{-1} runs, compaction stopped after a few meters of displacement and the sample thickness remained constant.

3.2. Runs employing velocity stepping at high velocities

Four velocity stepping experiments were conducted at high slip rates ($>10^{-3} \text{ ms}^{-1}$) on mixed gouges (Table 2). In hdr617, the gouge was sheared at 10^{-3} ms^{-1} until a μ_s of 0.31 was reached, upon which velocity was stepped up to 0.98 ms^{-1} within 0.1 s (Fig. 3a and b). Friction increased over a short displacement to a μ_p of 0.53 (which is lower than μ_p in the constant velocity ex-

periment hdr at 1 ms^{-1}). After reaching μ_p friction weakened to a μ_s of 0.04 after 60 s of slip.

The data of hdr617 (Fig. 3c) and hdr618, hdr619, and hdr620 (Fig. 3d–f) were fitted using the two state variable rate-and-state friction law as described in Section 2.3, using both the slip law and the aging law to model the state variable evolution (resulting parameters shown in Table 2). The data from hdr619 and hdr620 were corrected for a linear slip-weakening trend. The $a - b$ value was similar for the aging law and the slip law, and was around -0.04 for hdr617, hdr618, and hdr619, and larger (-0.2) for hdr620 (7×10^{-2} to $5 \times 10^{-1} \text{ ms}^{-1}$). The μ_1 for the latter experiment was also higher with 0.53 vs. 0.3. Critical slip distance d_{c1} ranged from 0.1–1 m, and d_{c2} from 1–27 m, both being significantly larger when using the slip law to describe the data. Both critical slip distances were significantly shorter for hdr620. For hdr617 and hdr618 the slip law (Ruina) seemed to be better able to reproduce the observed behavior (Fig. 3c and 3d).

3.3. Microstructural investigation of samples deformed at constant velocity

SEM-BSE images of microstructures of a selection of experiments on pure halite gouge in the range $10^{-7}\text{--}10^{-2} \text{ ms}^{-1}$ are shown in Fig. 4. In some cases, the microstructure was disturbed during unloading or resin impregnation, resulting in extra space between grains or along the principal slip surface showing as black in the BSE images. In the sample that was deformed at 10^{-7} ms^{-1} (hdr622) evidence of cataclasis is observed (Fig. 4a and b); grains are fractured (I) and poorly sorted comminuted grains ($<10 \mu\text{m}$) had accumulated in a broad zone near the top gabbro wallrock (II). Also, grains are compacted together, showing indentations (III) and elongated grains boundaries (IV). A weak alignment of grains at an angle of $\sim 30^\circ$ to the wallrock can be observed. Grains on

Table 2

List of velocity stepping experiments and parameters obtained from rate-and-state fitting. With state law indicating which state variable law was used for the fit (Dieterich: aging law, Ruina: slip law) reference velocity V_1 and step velocity V_2 , steady state friction coefficient μ_1 at velocity V_1 , rate-and-state parameters a , b_1 and b_2 and $(a - b)$, critical slip distances d_{c1} and d_{c2} (see also Section 2.3).

Run #	State law	$V_1 - V_2$ (m s^{-1})	μ_1 (-)	a (-)	b_1 (-)	b_2 (-)	d_{c1} (m)	d_{c2} (m)	$a - b$ (-)
hdr617	Dieterich	$1 \times 10^{-3} \rightarrow 9.8 \times 10^{-1}$	0.31	0.0179	0.0411	0.0166	0.319	5.721	-0.040
hdr617	Ruina	$1 \times 10^{-3} \rightarrow 9.8 \times 10^{-1}$	0.31	0.0253	0.0467	0.0211	1.04	26.8	-0.043
hdr618	Dieterich	$1 \times 10^{-3} \rightarrow 8.7 \times 10^{-1}$	0.32	0.0274	0.0352	0.0312	0.144	1.79	-0.039
hdr618	Ruina	$1 \times 10^{-3} \rightarrow 8.7 \times 10^{-1}$	0.32	0.0326	0.0346	0.0380	0.446	6.66	-0.040
hdr619 ^a	Dieterich	$3 \times 10^{-2} \rightarrow 4.7 \times 10^{-1}$	0.30	0.0611	0.0646	0.040	0.630	3.14	-0.044
hdr619 ^a	Ruina	$3 \times 10^{-2} \rightarrow 4.7 \times 10^{-1}$	0.30	0.0654	0.0586	0.0507	1.17	5.23	-0.044
hdr620 ^a	Dieterich	$7 \times 10^{-2} \rightarrow 5.1 \times 10^{-1}$	0.53	0.0920	0.186	0.108	0.127	1.03	-0.20
hdr620 ^a	Ruina	$7 \times 10^{-2} \rightarrow 5.1 \times 10^{-1}$	0.53	0.0971	0.191	0.110	0.235	1.81	-0.20

^a A linear slip-weakening weakening trend was removed from of these experiments, -0.00265 m^{-1} for hdr619 and -0.001 m^{-1} for hdr620.

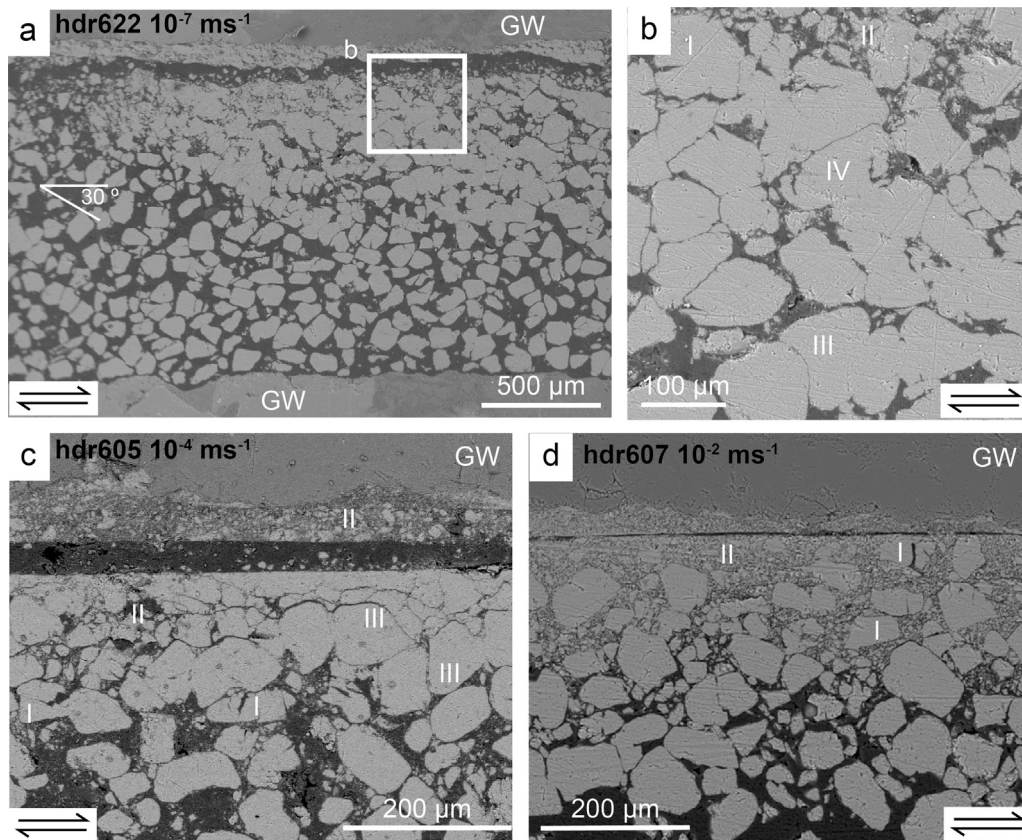


Fig. 4. SEM-BSE images of microstructures of pure halite samples deformed at velocities from 10^{-7} – 10^{-2} ms^{-1} . With a) hdr622, deformed at 10^{-7} ms^{-1} , b) a zoomed-in view of a, c) hdr605, deformed at 10^{-4} ms^{-1} , and d) hdr607, sheared at 10^{-2} ms^{-1} . The sense of shear is indicated by the arrows, and the scale is indicated by the white bar. GW: gabbro wall rock piston, I: fractured grain, II: comminuted grains, III: grain indentations and IV: compacted grains and elongated grain boundaries.

the bottom part appear to be unaffected by the deformation as they have similar grain size compared to the original material. At a faster slip rate of 10^{-4} ms^{-1} (hdr605), a sharp boundary shear formed with fine material ($<20 \mu\text{m}$) coating the wallrock surface (Fig. 4c). Immediately below the boundary shear grains are closer to their original size, and are compacted. In this zone similar phenomena are observed as in Fig. 4b, with fractured grains and grain comminution, indentations and strongly compacted grains. Further away from the boundary shear the grains appear undeformed. A sharp boundary shear also formed in the sample deformed at 10^{-2} ms^{-1} (hdr607) but more fine grained material was produced and accumulated in a broad zone on both sides of the boundary shear (Fig. 4c). Clasts are more angular and fractured compared to those in Fig. 4c, and no densely compacted grains are observed.

Microstructures of samples deformed in the higher velocity range (0.1 – 1 ms^{-1}) look distinctly different from those of the lower velocity samples; the original grains can no longer be recognized, microstructures are denser, and deformation is more pervasive throughout the sample (Fig. 5). Note that not only the velocity is higher, but the total amount of slip was also much larger than in the slower experiments (Table 1). The microstructure of the 0.1 ms^{-1} pure halite sample (Fig. 5a) contains fractured material of various sizes, ranging from clasts of $>200 \mu\text{m}$ (VI) which appear to be dense aggregates of finer material that were welded together, to more porous very fine material (μm scale). Two subhorizontal slipzones were present near the wallrocks (V), and smaller slipzones also run through the sample at an angle to the wallrock surface (VII), appearing to break up the denser clasts. The wallrock

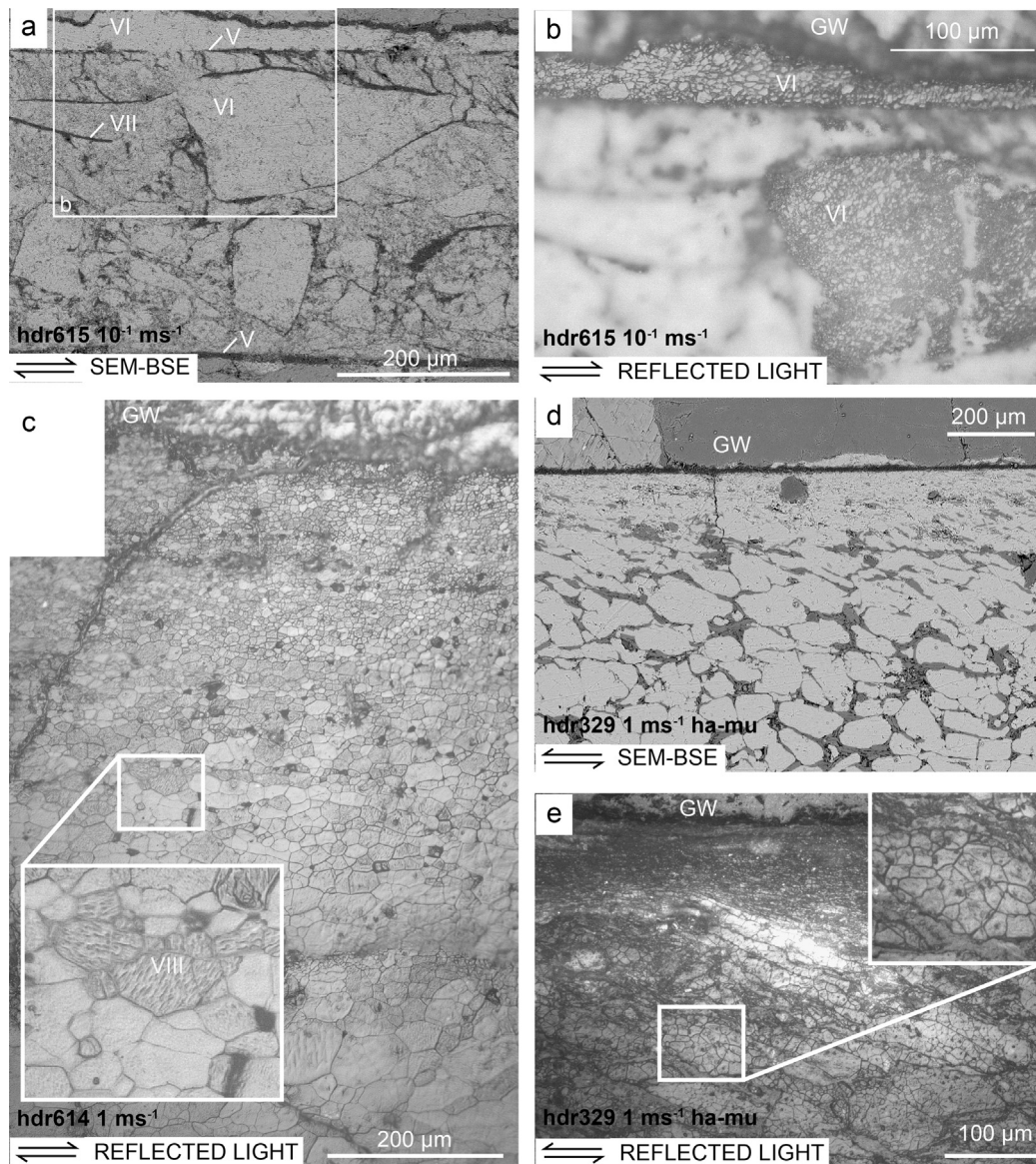


Fig. 5. SEM-BSE images and reflected light images of halite and halite-muscovite gouges deformed at slip rates 0.1–1 m s^{-1} . a) SEM-BSE image of pure halite gouge deformed at 0.1 m s^{-1} (hdr615), b) zoomed-in portion of a (see box in a) in reflected light, c) reflected light micrograph of pure halite deformed at 1 m s^{-1} (hdr614), d) SEM-BSE micrograph of halite-muscovite gouge deformed at 1 m s^{-1} (hdr329), e) reflected light image of d. Shear sense is indicated by the arrows. GW: gabbro wallrock, V: Y-shear, VI: dense agglomerated material, VII: fractures at an angle to sliding direction, VIII: (sub)grains containing lineations.

is coated with dense material similar to that of the dense clasts (VI). Reflected light micrographs showed the dense material had an internal structure of angular (sub)grains (Fig. 5b). Within the large clasts these recrystallized grains are equidimensional, close to the boundary shear they are slightly elongated. The pure halite sample deformed at 1 m s^{-1} shows a compact mass of equidimensional (sub)grains; virtually no porosity is present (Fig. 5c). A gradient in grain size from $\sim 40 \mu\text{m}$ at the bottom to $<5 \mu\text{m}$ at the top is visible. Some subgrains show slip lines indicative of internal dislocation (VIII), appearing darker in the micrograph, whereas others were lighter and more strain free. Areas of similarly colored subgrains might be indicative of old grain boundaries. The slip lines of some subgrains are oriented at a high angle to the slip lines of a neighboring grain and no evidence for grain boundary bulging is visible. Grain boundaries were mostly straight and triple junctions were sometimes observed. The microstructure of halite-muscovite deformed at the same slip rate of 1 m s^{-1} was more heterogeneous (Fig. 5d). A clear slip surface was present along the top wall-rock and elongated grains, separated by layers of muscovite,

were dragged into that slipping zone. In reflected light it was visible that the elongated grains contained subgrains with straight grain boundaries (Fig. 5e). Towards the slip surface grains contained increasingly more and smaller subgrains.

4. Discussion

The mechanical data of both halite and halite-muscovite gouges can be divided into four regimes as a function of slip rate, each with distinct slip- and velocity-dependent behavior of the steady state coefficient of friction μ_s (Fig. 6a). Friction was highest at the lowest velocities and decreased as slip rates increased. However at 10^{-1} m s^{-1} both pure halite and halite-muscovite samples showed re-strengthening. Friction dropped towards the lowest values of 0.05–0.1 at slip rates of 1 m s^{-1} . Towards the lowest velocities a transition to stable sliding and velocity-strengthening might have initiated, as indicated by the mechanical data of pure halite in Fig. 2a. The slip weakening distance D_w increased with increasing slip rate, from $\sim 0.01 \text{ m}$ to several meters at 1 m s^{-1} . Sample

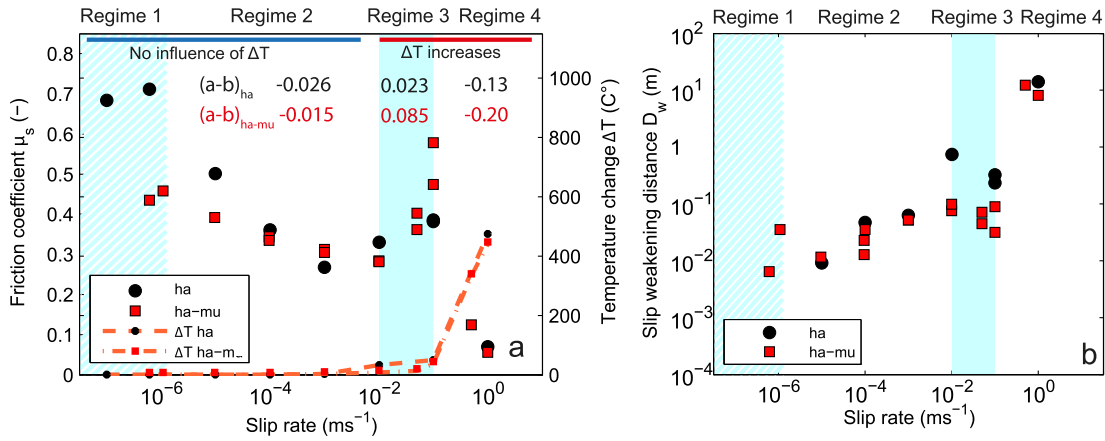


Fig. 6. Summary of steady state friction coefficients and critical slip distances as a function of slip rate. a) The evolution of the steady state friction coefficient μ_s with the applied slip rate v for pure halite (black dots) and halite-muscovite (red squares). For hardening samples (i.e. those sheared at 10^{-7} and 10^{-6} m s^{-1}) we plotted the lowest friction value recorded after peak friction. An estimate of sample temperature increase, computed using Equation (6) is given. Average $(a - b)$ values ($= \Delta\mu_s / \Delta \ln(V)$) are listed for each regime. b) The slip weakening distance D_w at which samples have weakened to 5% of the total weakening from peak friction to steady state, against slip rate. (For interpretation of the references to color in this figure legend, the reader is referred to the web version of this article.)

temperature at the slip surface ($z = 0$) after a slip of D_w was estimated assuming 1-D diffusion of the heat generated at the slip surface into the gabbro wallrock (Carslaw and Jaeger, 1959)

$$\Delta T \left(t = \frac{D_w}{V} \right) = \frac{1}{(2\rho c_p \sqrt{\pi \alpha_{th}})} \int_0^{\frac{D_w}{V}} \frac{\tau(t - \xi) v}{\sqrt{\xi}} e^{-\frac{z^2}{4\alpha_{th}\xi}} d\xi \quad (6)$$

where ΔT (K) is the temperature rise from room temperature, τ is the shear stress as a function of time (Pa), ρ is the density of gabbro (3000 kg m^{-3}), c_p is specific heat of gabbro ($1000 \text{ J kg}^{-1} \text{ }^\circ\text{C}^{-1}$) (Waples and Waples, 2004), v (m s^{-1}) is the sliding velocity, and α_{th} the thermal diffusivity of gabbro (0.8×10^{-6} at 200°C) (Durham et al., 1987). Note that this is a lower bound to the temperature estimate; if diffusion was purely governed by the halite layer the temperature increase would exceed 800°C at the highest velocities (using values from Kim et al., 2010).

The average velocity dependence $(a - b)$ of the various regimes can be derived from the constant velocity experiments using Equation (3). Critical slip distances as a function of slip rate are shown in Fig. 6b. Some data (in particular the high velocity data) show very rapid initial weakening, and could not be fit with Equation (1), and values for D_w and D_{th} were selected manually from smoothed data (see Table 1). This non-exponential behavior was observed for some other gouge materials as well (e.g. Yao et al., 2013).

4.1. Deformation mechanisms

For each of the four different regimes recognized from the mechanical data we analyze the microstructure and operative deformation mechanisms. The microstructures observed for the stably sliding pure halite samples in Regime 1 indicate the occurrence of cataclasis, and possibly deformation at an oblique angle (Riedel orientation) to the sliding direction (Fig. 4a). Also, grain compaction and indentations suggest pressure solution processes to have been operative, even at room-dry conditions (Fig. 4b). The observed compaction curves (compaction-dilatation-compaction, see Fig. 2a) are typical for loading of materials with a competition between pressure solution and cataclastic processes (Bos et al., 2000b; Niemeijer et al., 2010). Overall compaction rates are expected to decrease with time because porosity decreases and the contact area increases, lowering the stress and thus reducing pressure solution (Bos et al., 2000b). Rapid pressure solution of the initially porous gouge before peak friction can thus

explain the initial rapid compaction rates. Cataclasis, grain comminution and the onset of localization of slip along the top wall rock or along incipient Riedel shears can cause the weakening observed up to 1.5–2 mm following peak friction. The dilatancy observed during this phase is often observed during shear deformation of granular material (Marone, 1998; Marone et al., 1990; Beeler et al., 1996), and was stronger than the compaction rate at this stage of the experiment. Further localization up to 4–5 mm of slip would weaken samples further, but also reduce the dilatation rate, so that compaction of the bulk gouge could again become dominant. However, grain size reduction would also promote solution transfer processes, and could lead to strengthening of grain contacts through pressure solution. If this effect is strong enough it could increase the overall strength of the gouge (Beeler et al., 1996), prevent localization and cause more pervasive deformation of the gouge (Bos et al., 2000a). This could cause the reduced compaction rate and slip-hardening seen in later stages of the experiments in Regime 1. Gouge structure may change with increasing slip, and possibly continued slip could induce localization along a Y-shear (Marone, 1998); further experiments are required to investigate this issue. However, the behavior of pure halite at 20 mm of slip at 10^{-7} and 10^{-6} m s^{-1} is clearly different from the frictional behavior at higher slip rates. The mixed gouge deformed at 10^{-6} m s^{-1} behaved different from its stable pure halite equivalent, showing rapid weakening and stick-slip. Possibly the presence of phyllosilicates has prevented grain contacts from healing and strengthening of the gouge (Bos et al., 2000a).

Localized deformation as seen in Regime 2 (Fig. 4c) is often associated with the observed unstable slip and/or slip weakening behavior (Beeler et al., 1996; Marone, 1998; Niemeijer et al., 2010). Samples of both pure halite and mixed gouge showed rapid slip-weakening indicative of the observed localization, reaching steady state at 10–15 mm of displacement. The fine grained angular material points to cataclasis to be operative in the boundary shear (Fig. 4c). Rapid healing of that fine material through pressure solution explains the stick-slip behavior (Niemeijer et al., 2010), but slip rates may have been too fast for pressure-solution healing to cause strengthening and distributed deformation. The mixed gouge was weaker than the pure halite gouge. Phyllosilicates have a lower strength compared to most rocks; the lower μ_s of pure muscovite at low temperatures of around 0.4 (Van Diggelen et al., 2010) reduces the overall strength of the mixed gouge as seen in halite-muscovite experiments (Niemeijer and Spiers, 2005) and quartz-mica mixtures (e.g. Saffer and Marone, 2003). In Regime 2 (up to velocities of 10^{-4} m s^{-1}) the dilatation as observed in

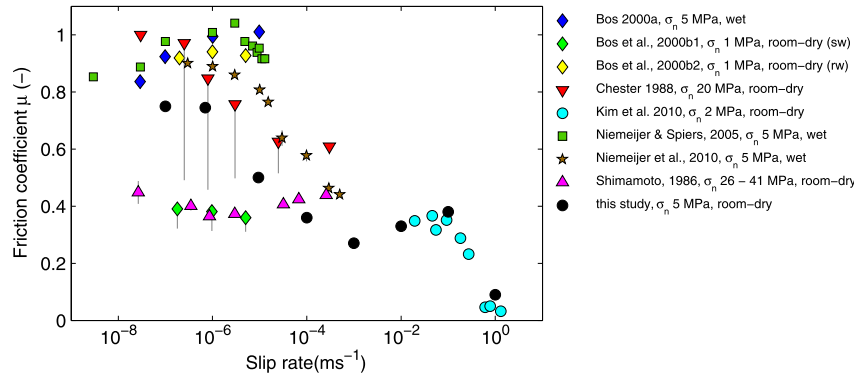


Fig. 7. Comparison of steady state friction coefficient of pure halite to data from other studies. References are indicated in the legend, with between brackets the applied normal stress and humidity. For Bos et al. (2000b) it is indicated whether smooth (sw) or rough wall-rocks (rw) were used. Vertical gray lines in the graph indicate the average size of the stick-slip events where observed. (For interpretation of the references to color in this figure, the reader is referred to the web version of this article.)

Regime 1 expressed itself as a stage of reduced compaction rate rather than net dilatation (Fig. 2a). The gouge may still have been relatively porous because less time was available for compaction in these faster experiments before reaching peak strength, causing compaction rates to be high. Rapid localization also causes less dilatation, leading to the relatively high compaction rate in Regime 2, which seems mainly to occur within the bulk gouge next to the boundary shear (Fig. 4c). We suggest friction in Regime 2 is governed by cataclastic processes in a localized boundary shear whereas the compaction signal is dominated by pressure-solution compaction of the bulk gouge.

The large dense clasts consisting of dynamically recrystallized grains, within a porous matrix of fractured fine material, reflect a transition from brittle to plastic processes as temperature start to increase in Regime 3. Rapid slip weakening in the first 0.1–1 m might still reflect brittle processes with cataclasis, grain size reduction and localization as in Regime 2, with temperature still $<100^\circ\text{C}$ at D_{th} . The amount of weakening at this amount of slip is less than observed in experiments in Regime 2. Slip rates are fast and shear heating might have caused (parts of) the material to coalesce via plastic processes preventing further localization. The influence of plastic processes is observed clearly in the final microstructure of hdr615 (arrested after several m of slip) where dense, strong aggregates are visible (Fig. 5). The recrystallization process forming the aggregates might have been too slow to keep up with the rapid deformation rate, so that it was re-fractured in a brittle manner. Several cycles of plastic and brittle deformation may be present, causing the irregular friction observed in the experiment (hdr615). It is difficult to draw strong conclusions from the microstructure, since gouge loss may have influenced the microstructure. The micrographs do however indicate that plastic deformation (diffusion or dislocation creep) processes start to play a role at these velocities and displacements. The higher the velocities, the higher the temperature and the more dominant the recrystallization. Even at smaller slip than achieved in hdr615, the extreme grain size reduction and rise of temperature could already activate plasticity, possibly explaining the velocity strengthening behavior. The muscovite-containing gouge actually became stronger than the pure halite gouge with a μ_s of 0.5 versus 0.4 at 0.1 ms^{-1} . Other studies show pure muscovite becomes stronger with temperature, up to 0.5 at $300\text{--}400^\circ\text{C}$ (Van Diggelen et al., 2010). The estimated ΔT at the final displacement using Equation (6) could exceed 500°C in a localized zone, so it may be that the stronger muscovite could raise the average strength of the gouge.

In regime 4 extreme slip and velocity weakening was observed, and the pure halite sample was entirely recrystallized. Other experiments on halite under similar conditions and velocities showed

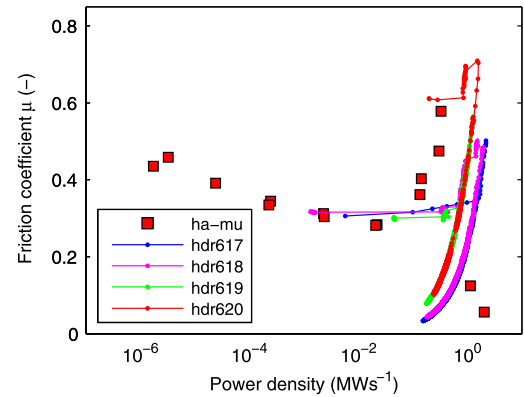


Fig. 8. Friction of constant velocity experiments and friction measured during a velocity step as a function of power density (shear stress \times slip rate). Steady-state friction reached in constant slip rate experiments on halite-muscovite gouge are indicated by the red squares. Friction measured upon imposing a velocity step for four experiments (see Table 2). (For interpretation of the references to color in this figure legend, the reader is referred to the web version of this article.)

the presence of melt in the principal slip zone (Kim et al., 2010). We have not found direct evidence for melting in our microstructure, but recrystallization may have erased the molten surface. We also did not find textures indicative for superplasticity in the slip zone, as were found in carbonates (De Paola et al., 2015), although (sub)grain sizes were very small in our samples (100 nm). High temperatures generated at a high strain rate on a principal slip surface could cause the neighboring halite to deform through dislocation/diffusion creep at lower strain rates. In case melt was present, the contribution of plastic creep at the slip surface or surrounding zone was probably minor due to the low viscosity of the melt. Molten halite has a low viscosity, $1.03 \times 10^{-3}\text{ Pa s}$ at 800°C (Janz, 1980) which could explain the observed low friction, but further research is required at different amounts of slip to determine the exact mechanisms that are active in the gouge. In Regime 4, muscovite-containing samples yielded foliated structure (Fig. 5f), and a gradient in the degree of recrystallization (increasing towards the slip surface) was observed which was different from the pure halite which had recrystallized over the entire sample. Muscovite may have acted as an insulator, preventing temperature to conduct further into the sample and thus prevent plastic deformation far away from the slip surface. Muscovite may also have prevented recrystallization after the experiments was terminated. Also for the muscovite-containing experiment melt nor textures indicative for plastic flow were found in the slip surface, but again a melt may have existed.

4.2. Comparison to other studies on halite gouges

The data obtained in this study agree well with frictional data on pure halite from most other studies at similar low normal stresses and room temperature, even though many different deformation apparatuses, wall rocks, halite grain sizes, and moisture conditions were used (Fig. 7). As in Regime 1 of this study, stable sliding at a friction of 0.7–1, cataclastic flow and distributed faulting of both wet and room-dry halite gouge were observed at the slowest slip rates (Niemeijer and Spiers, 2005; Bos et al., 2000a, 2000b; Chester, 1988; Niemeijer et al., 2010). Also, the transition to velocity-weakening and unstable sliding due to localized deformation along the wall-rock gouge interface was observed (Regime 2 in this study) at slip rates faster than 10^{-6} m s^{-1} (Niemeijer and Spiers, 2005; Niemeijer et al., 2010) or from slightly slower slip rates of $2.5 \times 10^{-7} \text{ m s}^{-1}$ (Chester, 1988), which may have been due to the higher normal stress. The $(a - b)$ values measured in velocity stepping experiments in halite (-0.08 – 0) (Niemeijer et al., 2010) are in line with the slope of the velocity dependence of friction obtained for the constant velocity experiments (-0.02 , see Fig. 6a).

Two datasets differed markedly in the Regime 1 and 2 velocity range, with a much lower coefficient of friction (0.35–0.45) and stick-slip behavior also at the lowest (10^{-8} – 10^{-6}) slip rates (Shimamoto, 1986; Bos et al., 2000b), and stable behavior at slip rates exceeding $3 \times 10^{-6} \text{ m s}^{-1}$ (Shimamoto, 1986). For the dataset of Bos et al. (2000b) the unstable behavior was related to the smoother steel wall rocks used (30 μm teeth, green diamonds in Fig. 7), which promoted localization and unstable slip, whereas rougher (500 μm teeth, yellow diamonds in Fig. 7) wall-rocks caused stable sliding. Gabbro wall-rocks used in this study were also smooth (~ 10 – $30 \mu\text{m}$ relief), yet halite gouge did show stable sliding at slip rates up to 10^{-6} m s^{-1} . Possibly differences in wall-rock stiffness or normal stress could be the cause of the different behavior, but more likely it could be that the moisture content of the room-dry gouges in this study is higher, which would promote stable sliding at high friction (for moisture contents $>35\%$) even though wall-rocks are smooth (Bos et al., 2000b). In the experiments conducted by Shimamoto (1986) granular halite was precompacted at 200 MPa so that the starting material was a densely compacted aggregate. This would inhibit cataclastic flow and intergranular processes, and promote the observed localization along the wall-rock interface (Hiraga and Shimamoto, 1987), causing unstable sliding. No distinct deformation mechanism was recognized that caused stable sliding above $3 \times 10^{-6} \text{ m s}^{-1}$ (Hiraga and Shimamoto, 1987); perhaps the higher normal stress gave rise to different behavior at large slip rates.

Friction coefficients of room-dry halite measured by Kim et al. (2010) are in excellent agreement with our values in Regime 3 and 4, also showing a peak in friction at 0.1 m s^{-1} . Evidence for halite melting in a thin localized layer, flanked by a dynamically recrystallized zone, was reported by these authors at the velocities of Regime 4. The microstructures in the current study were however different; evidence of molten material and halite ribbon-like features were missing at 1 m s^{-1} which may be due to recrystallization. Possibly the different sample materials (pure halite vs. iodized cooking salt) can explain differences in recrystallization behavior and resulting microstructure.

4.3. Halite as an analog for quartzitic fault rock at in-situ conditions from low to high velocity

The observed strengthening–weakening–strengthening–weakening with increasing slip rate may have large implications for nucleation and propagation of earthquake rupture (Bar Sinai et al., 2012). Here we compare the observed strength evolution of halite

to that of other materials deformed at a range of conditions relevant to the upper crust.

Towards the slowest velocities halite gouges showed a transition to stable, velocity-strengthening behavior. At similar slow slip rates (and/or high temperatures) velocity-strengthening behavior and stable sliding was recognized in wet quartz (Niemeijer et al., 2008), and wet granite gouges (Blanpied et al., 1995, 1998), as a result of enhanced pressure-solution creep processes. At faster slip rates (a transition to) velocity-weakening behavior (Regime 2 for the halite data) was also observed in quartz (Goldsby and Tullis, 2002; Niemeijer et al., 2008; Ohashi et al., 2013), illite-quartz (den Hartog et al., 2012), and granite (Reches and Lockner, 2010; Liao et al., 2014) gouges for a range of normal stress and temperature conditions. Significant strain was required to develop the localized Y-shear responsible for the unstable behavior, and the weakening increased with normal stress (Goldsby and Tullis, 2002; Niemeijer et al., 2008). The magnitude of the velocity dependence ($a - b$) measured in rocks at elevated temperature (where pressure-solution was active) was of similar order (-0.02) as found in halite (see Fig. 6a), in contrast to room-temperature experiments where pressure solution was not active and $(a - b)$ and also D_c are an order of magnitude lower (Blanpied et al., 1998). The use of halite analog thus gives consistent data in Regimes 1 and 2 compared to quartz-rich fault rock at hydrothermal conditions where cataclasis and pressure solution were active, although the exact transition from strengthening to weakening will likely vary depending on normal stress and temperature (den Hartog and Spiers, 2013).

Strengthening at higher (sub-seismic) slip rates (~ 0.01 – 0.1 m s^{-1}) was observed in many rock types, including quartz and quartz-graphite (Ohashi et al., 2013), granite (Reches and Lockner, 2010; Liao et al., 2014), and dry clay-rich gouge (Ferri et al., 2011). All of these experiments were conducted under low normal stress, initial room-temperature, dry conditions, and constant velocity. The mechanisms of the restrengthening are not always clear, but Reches and Lockner (2010) find that agglomeration of grains is likely responsible, similar to what was found in this study. Another mechanism is the dehydration of clay material which increases the overall strength of the gouge (Ferri et al., 2011). These authors also find that in wet clays the strengthening is absent due to different weakening mechanisms (thermal pressurization) playing a role. The strengthening might be a characteristic of dry friction altogether (Bar Sinai et al., 2012). It is unclear whether similar mechanisms as observed in halite (agglomeration of grains, recrystallization) would be operative under in-situ conditions, and whether the strengthening at sub-seismic velocities would play a role during transient rupture (see Section 4.4).

All rock types deformed at high velocity (Regime 4) exhibit dramatic weakening, and a variety of weakening mechanisms have been proposed (Di Toro et al., 2011; Han et al., 2007; Hirose and Shimamoto, 2005). The exact deformation mechanism in our samples could not be identified, but localized melting of halite may have occurred (see Section 4.1). Lower normal stresses often used in high velocity experiments might promote more brittle processes in quartz-rich rock, such as powder lubrication (Di Toro et al., 2004, 2011; Han et al., 2010). Unfortunately high-velocity experiments could not be conducted at in-situ conditions, and the deformation mechanisms of quartz-rich rock at hydrothermal conditions and high velocities are currently not known. It is unclear how the halite data compares to those, but evidence from natural faults showed that quartzitic fault rock may have melted during coseismic slip, and the host rock plastically deformed, which is in agreement with the observations in halite at low normal stress (Bestmann et al., 2011).

In general, it seems changes in friction (strong–weak–restrengthening–weak) with velocity observed in halite is relevant to frictional behavior of quartzitic fault rocks under hydrothermal

conditions, though the re-strengthening region in Regime 3 must be analyzed further. Also, the effect of a transient velocity function (rather than constant velocity sliding) needs to be investigated, which is discussed in the next section.

4.4. Implications of constant velocity experiments and velocity stepping experiments

In many studies including this one the imposed deformation rate is kept constant for a certain distance. However, during natural earthquakes the slip rate is governed by stress, elastic strain energy, and (the evolution of) shear stress, and evidence suggests rupture may be propagating as a pulse, rapidly increasing in velocity and then slowly decreasing in velocity (Heaton, 1990; Noda and Lapusta, 2013). Friction under such velocity conditions may evolve very different from that observed in constant velocity experiments (Liao et al., 2014). To discuss this, we compare the data of velocity stepping experiments (representative for the rapid initial acceleration of a propagating pulse) to the constant velocity experiments, plotted as a function of power density (shear stress \times velocity) in Fig. 8 (Di Toro et al., 2011). After stepping the velocity up (a three order of magnitude change was achieved within 0.1 s, see Section 3.2) friction increased to ~ 0.5 , and then decreased to values similar to those observed in the constant velocity experiments. The $(a - b)$ values are all negative for these steps, which step from or over the velocity-strengthening Regime 3 into the weakening Regime 4. It seems this re-strengthening at 10^{-1} ms^{-1} did not affect greatly the overall weakening behavior. The displacement at this velocity is very small during the step (contrary to the constant velocity experiments) and the final velocity is determining for the observed weakening. However, the re-strengthening regime and the onset of plastic processes might have contributed to the initial strengthening after the velocity step. The observation of this initial strengthening is different from findings by Liao et al. (2014) who stepped the velocity starting from lower slip rates where the gouge was relatively strong. They found that the weakening-strengthening behavior observed at intermediate velocities in constant velocity experiments disappeared, and gouges barely strengthened before showing rapid weakening. Here, we started from a low strength, and do find initial strengthening when the velocity is stepped up, followed by rapid weakening. This implies that the initial frictional strength of the fault (and thus the initial slip rate), and possibly the friction behavior at the velocities spanned by the step, may influence the subsequent evolution of friction (in particular the a -value, which describes the instantaneous response to a velocity step) upon sudden acceleration.

Whether the observed velocity-strengthening and weakening regimes observed in the constant velocities play a role under transient velocities is important for modeling of rupture. A velocity-dependent $(a - b)$ value may give rise to different slip phenomena, such as slow slip and episodic tremor (Shibazaki and Shimamoto, 2007; Hawthorne and Rubin, 2013), and subseismic strengthening mechanisms may act as a barrier to accelerating slip. The subseismic strengthening regime also depends on the active deformation mechanisms; for clay-rich materials where dehydration reactions and thermal pressurization play a role strengthening at subseismic velocities is not observed and friction is low (~ 0.2) at constant velocities $< 0.1 \text{ ms}^{-1}$ and shows a small drop to a friction of 0.05–0.1 at 1 ms^{-1} (Ferri et al., 2011; Ujiie and Tsutsumi, 2010). We suggest further research into the transient properties of friction using realistic velocity functions on materials that exhibit the relevant deformation mechanisms for fault rocks at depth.

The experiments at high-velocity (both stepping and constant velocity experiments) did not show the exponential evolution as is often observed in high-velocity experiments (Mizoguchi et al., 2007; Sone and Shimamoto, 2009), but a better fit to the veloc-

ity steps was achieved by using a two-state variable rate-and-state friction model. The two critical slip distances obtained from the fit may reflect the different mechanisms to be operative. This is confirmed by the constant velocity experiments which also show how D_w is dependent on slip rate and the mechanism of deformation, which changes with increasing velocity (and displacement). Note that the absolute magnitude of $(a - b)$ (down to -0.22) is much larger than for slow experiments, and RSF results from slow experiments may not be extrapolated to high velocities where different mechanisms are at work. Microphysical models capturing the relevant processes would be required to extrapolate $(a - b)$ observed in the low velocity regime.

5. Conclusions

In this research, we investigated the frictional properties of analogue halite and halite–muscovite gouge from very slow slip rates of 10^{-7} ms^{-1} to seismic slip rates of 1 ms^{-1} . A total number of 23 experiments were run at constant sliding velocity, and in 6 experiments the velocity was changed up to three orders of magnitude in the high-velocity regime (10^{-3} – 1 ms^{-1}). Four regimes were recognized from the mechanical data, each characterized by distinctly different mechanical behavior and deformation mechanisms, and are defined as:

- Regime 1 (10^{-7} – 10^{-6} ms^{-1}): Pure halite samples were relatively strong (μ_s 0.8–0.9), exhibited slip-weakening followed by slip-hardening (Fig. 2a), and the μ was velocity-independent or -strengthening (Fig. 6a). Deformation occurred through cataclasis, pressure-solution, and distributed deformation.
- Regime 2 (10^{-6} – 10^{-3} ms^{-1}) showed for both gouge compositions rapid slip weakening, the absence of dilatation, stick-slips and a decrease of μ_s with sliding velocity to ~ 0.3 at 10^{-3} ms^{-1} . Average $(a - b)$ values in this regime of -0.026 and -0.018 were computed for pure halite and halite–muscovite, respectively. D_w increased with slip rate from 0.01 to 0.06 m. Microstructures showed highly localized boundary shears and grain compaction near these shear zones.
- In Regime 3 ($\sim 10^{-2}$ – 10^{-1} ms^{-1}) samples became stronger with increasing slip rate with average $(a - b)$ values of 0.023 and 0.098, reaching a μ_s of 0.4 for pure halite and 0.57 for the halite–muscovite mixture at 10^{-1} ms^{-1} . Initially, sample strength decreased with slip, but at higher displacements, phases of restrengthening and weakening were observed in the mechanical data. Samples likely initially deformed through cataclasis and localization, but as temperature started to play a role the small grains formed large strong agglomerates which restrengthened the gouge.
- Regime 4 (10^{-1} – 1 ms^{-1}) is characterized by extreme slip and velocity weakening. From 0.1 to 1 ms^{-1} $(a - b)$ reaches values of -0.14 for the pure halite samples and -0.22 for halite–muscovite, and D_w was significantly larger than at slower slip rates, ranging up to $> 10 \text{ m}$. Microstructures of pure halite showed recrystallized grains throughout the sample. The microstructure of the halite–muscovite gouge showed a boundary shear zone, with plastically grains dragged into this shear zone, becoming increasingly deformed towards it.

Other findings are:

- The data were in good agreement with most other halite data from low and high velocity experiments, and bridged the gap between low and high velocity experimental data.
- The slip weakening distance D_w increased from $\sim 0.01 \text{ m}$ at a slip rate of 10^{-6} ms^{-1} to 10–20 m at 1 ms^{-1} . Different

(thermally-activated) deformation mechanisms may result in different values of D_w .

- Large velocity steps from 10^{-3} to 1 ms^{-1} showed initial strengthening followed by rapid weakening. The steps could be modeled using a two-state-variable rate-and-state friction model (they could not be fit by an exponential model) even though different mechanism are operative compared to low velocity friction experiments.
- The initial friction level from which velocity is stepped could affect the frictional response during the step, in particular the initial strengthening upon acceleration.

The different velocity-strengthening and velocity-weakening regimes as a function of velocity could have significant effect on rupture propagation and radiated seismic waves. Also the two length-scales recognized in the velocity stepping experiments from low to seismic velocity will affect the nucleation process of earthquakes.

Acknowledgements

We thank Peter van Krieken at Utrecht University for his help with gouge preparation and microstructural work. We also thank various colleagues at Utrecht University and Hiroshima University for their helpful discussions. André Niemeijer is funded by European Research Council starting grant SEISMIC (335915) and the Netherlands Organisation for Scientific research (NWO) VIDI grant (Nr. 854.12.011). We thank Nicola De Paola and Matt Ikari for their constructive reviews.

References

- Bar Sinai, Y., Brener, E.A., Bouchbinder, E., 2012. Slow rupture of frictional interfaces. *Geophys. Res. Lett.* 39 (3), L03308.
- Beeler, N.M., Tullis, T.E., Blanpied, M.L., Weeks, J.D., 1996. Frictional behavior of large displacement experimental faults. *J. Geophys. Res., Solid Earth* 101 (B4), 8697–8715.
- Ben-Zion, Y., Rice, J.R., 1997. Dynamic simulations of slip on a smooth fault in an elastic solid. *J. Geophys. Res., Solid Earth* 102 (B8), 17771–17784.
- Bestmann, M., Pennacchioni, G., Frank, G., Göken, M., de Wall, H., 2011. Pseudotachylite in muscovite-bearing quartzite: coseismic friction-induced melting and plastic deformation of quartz. *J. Struct. Geol.* 33 (2), 169–186.
- Blanpied, M.L., Lockner, D.A., Byerlee, J.D., 1995. Frictional slip of granite at hydrothermal conditions. *J. Geophys. Res., Solid Earth* 100 (B7), 13045–13064.
- Blanpied, M.L., Marone, C.J., Lockner, D.A., Byerlee, J.D., King, D.P., 1998. Quantitative measure of the variation in fault rheology due to fluid-rock interactions. *J. Geophys. Res., B, Solid Earth* 103 (5), 9691–9712.
- Bos, B., Peach, C.J., Spiers, C.J., 2000a. Frictional-viscous flow of simulated fault gouge caused by the combined effects of phyllosilicates and pressure solution. *Tectonophysics* 327 (3–4), 173–194. 12/15.
- Bos, B., Peach, C.J., Spiers, C.J., 2000b. Slip behavior of simulated gouge-bearing faults under conditions favoring pressure solution. *J. Geophys. Res., Solid Earth* 105 (B7), 16699–16717.
- Carlsaw, H.S., Jaeger, J.C., 1959. *Conduction of Heat in Solids*, 2nd edition. Clarendon Press, Oxford.
- Chester, F.M., 1988. The brittle–ductile transition in a deformation-mechanism map for halite. *Tectonophysics* 154 (1–2), 125–136.
- Chester, F.M., Logan, J.M., 1990. Frictional Faulting in Polycrystalline Halite: Correlation of Microstructure, Mechanisms of Slip, and Constitutive Behavior. *The Brittle-Ductile Transition in Rocks*. American Geophysical Union, pp. 49–65.
- De Paola, N., Holdsworth, R.E., Viti, C., Collettini, C., Bullock, R., 2015. Can grain size sensitive flow lubricate faults during the initial stages of earthquake propagation? *Earth Planet. Sci. Lett.* 431, 48–58.
- den Hartog, S.A.M., Peach, C.J., de Winter, D.A.M., Spiers, C.J., Shimamoto, T., 2012. Frictional properties of megathrust fault gouges at low sliding velocities: new data on effects of normal stress and temperature. *J. Struct. Geol.* 38, 156–171.
- den Hartog, S.A.M., Spiers, C.J., 2013. Influence of subduction zone conditions and gouge composition on frictional slip stability of megathrust faults. *Tectonophysics* 600, 75–90.
- Di Toro, G., Goldsby, D.L., Tullis, T.E., 2004. Friction falls towards zero in quartz rock as slip velocity approaches seismic rates. *Nature* 427 (6973), 436–439.
- Di Toro, G., Han, R., Hirose, T., De Paola, N., Nielsen, S., Mizoguchi, K., et al., 2011. Fault lubrication during earthquakes. *Nature* 471 (7339), 494–498.
- Dieterich, J.H., 1979. Modeling of rock friction. 1. Experimental results and constitutive equations. *J. Geophys. Res.* 84, 2161.
- Durham, W.B., Mirkovich, V.V., Heard, H.C., 1987. Thermal diffusivity of igneous rocks at elevated pressure and temperature. *J. Geophys. Res., Solid Earth* 92 (B11), 11615–11634.
- Ferri, F., Di Toro, G., Hirose, T., Han, R., Noda, H., Shimamoto, T., et al., 2011. Low- to high-velocity frictional properties of the clay-rich gouges from the slipping zone of the 1963 Vaiont slide, northern Italy. *J. Geophys. Res., Solid Earth* 116 (B9), B09208.
- Goldsby, D.L., Tullis, T.E., 2002. Low frictional strength of quartz rocks at subseismic slip rates. *Geophys. Res. Lett.* 29 (1), 1844.
- Han, R., Shimamoto, T., Hirose, T., Ree, J., Ando, J., 2007. Ultralow friction of carbonate faults caused by thermal decomposition. *Science* 316 (5826), 878–881.
- Han, R., Hirose, T., Shimamoto, T., 2010. Strong velocity weakening and powder lubrication of simulated carbonate faults at seismic slip rates. *J. Geophys. Res., Solid Earth* 115 (B3), B03412.
- Hawthorne, J.C., Rubin, A.M., 2013. Laterally propagating slow slip events in a rate and state friction model with a velocity-weakening to velocity-strengthening transition. *J. Geophys. Res., Solid Earth* 118 (7), 3785–3808.
- Heaton, T.H., 1990. Evidence for and implications of self-healing pulses of slip in earthquake rupture. *Phys. Earth Planet. Inter.* 64 (1), 1–20.
- Hiraga, H., Shimamoto, T., 1987. Textures of sheared halite and their implications for the seismogenic slip of deep faults. *Tectonophysics* 144 (1–3), 69–86.
- Hirose, T., Shimamoto, T., 2005. Growth of molten zone as a mechanism of slip weakening of simulated faults in gabbro during frictional melting. *J. Geophys. Res., Solid Earth* 110 (B5), B05202.
- Janz, G.J., 1980. Molten salts data as reference standards for density, surface tension, viscosity, and electrical conductance: KNO₃ and NaCl. *J. Phys. Chem. Ref. Data* 9 (4), 791–830.
- Kim, J., Ree, J., Han, R., Shimamoto, T., 2010. Experimental evidence for the simultaneous formation of pseudotachylite and mylonite in the brittle regime. *Geology* 38 (12), 1143–1146.
- Lapusta, N., Rice, J.R., Ben-Zion, Y., Zheng, G., 2000. Elastodynamic analysis for slow tectonic loading with spontaneous rupture episodes on faults with rate- and state-dependent friction. *J. Geophys. Res., Solid Earth* 105 (B10), 23765–23789.
- Liao, Z., Chang, J.C., Reches, Z., 2014. Fault strength evolution during high velocity friction experiments with slip-pulse and constant-velocity loading. *Earth Planet. Sci. Lett.* 406, 93–101.
- Marone, C., 1998. Laboratory-derived friction laws and their application to seismic faulting. *Annu. Rev. Earth Planet. Sci.* 26, 643.
- Marone, C., Raleigh, C.B., Scholz, C.H., 1990. Frictional behavior and constitutive modeling of simulated fault gouge. *J. Geophys. Res., Solid Earth* 95 (B5), 7007–7025.
- Mizoguchi, K., Hirose, T., Shimamoto, T., Fukuyama, E., 2007. Reconstruction of seismic faulting by high-velocity friction experiments: an example of the 1995 Kobe earthquake. *Geophys. Res. Lett.* 34 (L01308).
- Niemeijer, A.R., Spiers, C.J., 2005. Influence of phyllosilicates on fault strength in the brittle–ductile transition: insights from rock analogue experiments. In: Bruhn, D., Burlini, L. (Eds.), *High-strain Zones: Structure and Physical Properties*. In: Special Publication Ed. Geological Society of London, p. 303.
- Niemeijer, A.R., Spiers, C.J., 2006. Velocity dependence of strength and healing behaviour in simulated phyllosilicate-bearing fault gouge. *Tectonophysics* 427, 231.
- Niemeijer, A.R., Spiers, C.J., Peach, C.J., 2008. Frictional behaviour of simulated quartz fault gouges under hydrothermal conditions: results from ultra-high strain rotary shear experiments. *Tectonophysics* 460 (1–4), 288–303.
- Niemeijer, A., Marone, C., Elsworth, D., 2010. Frictional strength and strain weakening in simulated fault gouge: competition between geometrical weakening and chemical strengthening. *J. Geophys. Res., Solid Earth* 115 (B10), B10207.
- Noda, H., Lapusta, N., 2013. Stable creeping fault segments can become destructive as a result of dynamic weakening. *Nature* 493 (7433), 518–521.
- Oohashi, K., Hirose, T., Shimamoto, T., 2013. Graphite as a lubricating agent in fault zones: an insight from low- to high-velocity friction experiments on a mixed graphite-quartz gouge. *J. Geophys. Res., Solid Earth* 118 (5), 2067–2084.
- Reches, Z., Lockner, D.A., 2010. Fault weakening and earthquake instability by powder lubrication. *Nature* 467 (7314), 452–455.
- Reinen, L.A., Weeks, J.D., 1993. Determination of rock friction constitutive parameters using an iterative least squares inversion method. *J. Geophys. Res., Solid Earth* 98 (B9), 15937–15950.
- Ruina, A., 1983. Slip instability and state variable friction laws. *J. Geophys. Res.* 88 (370), 10.
- Saffer, D.M., Marone, C., 2003. Comparison of smectite- and illite-rich gouge frictional properties: application to the updip limit of the seismogenic zone along subduction megathrusts. *Earth Planet. Sci. Lett.* 215 (1–2), 219–235.
- Shibazaki, B., Shimamoto, T., 2007. Modelling of short-interval silent slip events in deeper subduction interfaces considering the frictional properties at the unstable–stable transition regime. *Geophys. J. Int.* 171 (1), 191–205.
- Shimamoto, T., 1985. The origin of large or great thrust-type earthquakes along subducting plate boundaries. *Tectonophysics* 119 (1–4), 37–65.
- Shimamoto, T., 1986. Transition between frictional slip and ductile flow for halite shear zones at room temperature. *Science* 231 (4739), 711–714.

- Sone, H., Shimamoto, T., 2009. Frictional resistance of faults during accelerating and decelerating earthquake slip. *Nat. Geosci.* 2 (10), 705–708.
- Togo, T., Shimamoto, T., 2012. Energy partition for grain crushing in quartz gouge during subseismic to seismic fault motion: an experimental study. *J. Struct. Geol.* 5 (38), 139–155.
- Tsutsumi, A., Shimamoto, T., 1997. High-velocity frictional properties of gabbro. *Geophys. Res. Lett.* 24 (6), 699–702.
- Ujiie, K., Tsutsumi, A., 2010. High-velocity frictional properties of clay-rich fault gouge in a megasplay fault zone, Nankai subduction zone. *Geophys. Res. Lett.* 37 (24).
- Van Diggelen, E.W.E., De Bresser, J.H.P., Peach, C.J., Spiers, C.J., 2010. High shear strain behaviour of synthetic muscovite fault gouges under hydrothermal conditions. *J. Struct. Geol.* 32 (11), 1685–1700.
- Waples, D., Waples, J., 2004. A review and evaluation of specific heat capacities of rocks, minerals, and subsurface fluids. Part 1: Minerals and nonporous rocks. *Nat. Resour. Res.* 13 (2), 97–122.
- Yao, L., Ma, S., Shimamoto, T., Togo, T., 2013. Structures and high-velocity frictional properties of the Pingxi fault zone in the Longmenshan fault system, Sichuan, China, activated during the 2008 Wenchuan earthquake. *Tectonophysics* 599, 135–156.